# Compressible Magnetohydrodynamic Turbulence Modulated by Collisionless Damping in Earth's Magnetosheath: Observation Matches Theory

Siqi Zhao,[1] Huirong Yan,[1,*] Terry Z. Liu,[2,†] Ka Ho Yuen,[3] and Mijie Shi[4]

[1] *Deutsches Elektronen Synchrotron DESY, Platanenallee 6, D-15738, Zeuthen, Germany*
*Institut für Physik und Astronomie, Universität Potsdam, D-14476, Potsdam, Germany*
[2] *Department of Earth, Planetary, and Space Sciences, University of California, Los Angeles, CA 90024, USA*
[3] *Theoretical Division, Los Alamos National Laboratory, Los Alamos, NM 87545, USA*
[4] *Shandong Key Laboratory of Optical Astronomy and Solar-Terrestrial Environment, Institute of Space Sciences, 264209, Shandong University, Weihai, People's Republic of China*

(Dated: submitted to PRL on May 11, 2023)

In this letter, we provide the first observational evidence of substantial collisionless damping (CD) modulation in the magnetohydrodynamic (MHD) turbulence cascade in Earth's magnetosheath using four *Cluster* spacecraft. Plasma turbulence is primarily shaped by the forcing on large scales and damping on small scales. Based on an improved compressible MHD decomposition algorithm, our observations demonstrate that CD enhances the anisotropy of compressible MHD modes due to their strong pitch angle dependence. The wavenumber distributions of slow modes are more stretched perpendicular to the background magnetic field ($\mathbf{B_0}$) under CD modulation compared to Alfvén modes. In contrast, fast modes are subject to a more significant CD modulation. Fast modes exhibit a scale-independent, slight anisotropy above the CD truncation scales, and their anisotropy increases as the wavenumbers fall below the CD truncation scales. As a result, CD affects the relative energy fractions in total compressible modes. Our findings take a significant step forward in comprehending the functions of CD in truncating the compressible MHD turbulence cascade and the consequential energy anisotropy in the wavevector space.



*Introduction.*— Plasma turbulence, particularly its compressible component, plays a crucial role in numerous astrophysical processes, such as the heating and acceleration of solar wind, cosmic ray transport, and star formation [1–4]. The current model of plasma turbulence is typically characterized by a three-way process: (1) energy injection on large scales [5, 6], (2) inertial energy cascade following some self-similar power law scaling, and (3) dissipation caused by certain kinetic physical processes on small scales [7, 8]. Inertial energy cascade, the most characteristic signature of magnetohydrodynamic (MHD), has been effectively described using incompressible MHD models such as the isotropic theory (IK65) [9, 10] and scale-dependent anisotropic turbulence theory (GS95) [11]. The nearly incompressible (NI) theory has also been used to explain some phenomena related to compressible solar wind turbulence [12, 13]. However, compressible MHD turbulence is subjected to various damping processes while following the inertial energy cascade [14–17], which is still not completely understood. Fully comprehending how damping truncates compressible MHD turbulence is an inseparable piece for depicting turbulence in real astrophysical plasma.

The anisotropy of compressible turbulence in the inertial range has been extensively studied through simulations and satellite observations [18, 19]. In a homogeneous plasma with a uniform background magnetic field ($\mathbf{B_0}$), small amplitude compressible MHD fluctuations can be decomposed into three MHD eigenmodes (namely, Alfvén, slow, and fast modes) [20–25]. The linear independence among the three MHD eigenmodes enables individual analysis of their statistical properties in the small amplitude limit [21, 26]. The mode composition of MHD turbulence significantly affects the energy cascade and observational turbulence statistics [23, 27–29]. Based on current compressible turbulence models, Alfvén and slow modes are expected to follow a cascade with scale-dependent anisotropy $k_\parallel \propto k_\perp^{2/3}$, where $k_\perp$ and $k_\parallel$ are wavenumbers perpendicular and parallel to $\mathbf{B_0}$ [11, 30]. In contrast, fast modes are expected to show isotropic behaviors and cascade like the acoustic wave [31, 32]. These theoretical conjectures have been confirmed by numerical simulations [23, 26].

Earlier theoretical studies have demonstrated a strong propagation angle dependence in collisionless and viscous damping, influencing the three-dimensional (3D) energy distributions [16, 33–35]. The collisionless damping (CD) leads to the rapid dissipation of plasma waves by the wave-particle interactions via gyroresonance or Landau resonance. Despite theoretical predictions, direct observations demonstrating how CD modulates the statistics of compressible MHD modes are still lacking, primarily due to the limited satellite measurements. Thanks to the availability of spatial information from four *Cluster* spacecraft, this letter presents the first observational evidence of substantial CD modulation in the compressible MHD turbulence cascade by comparing the CD rate predicted by theory with the compressible energy distributions measured by the *Cluster* mission.

*Overview.*— Fig. 1 shows an overview of *Cluster* observations in Earth's magnetosheath during 19:00-14:00 UT on 2-3 December 2003 in Geocentric Solar Ecliptic

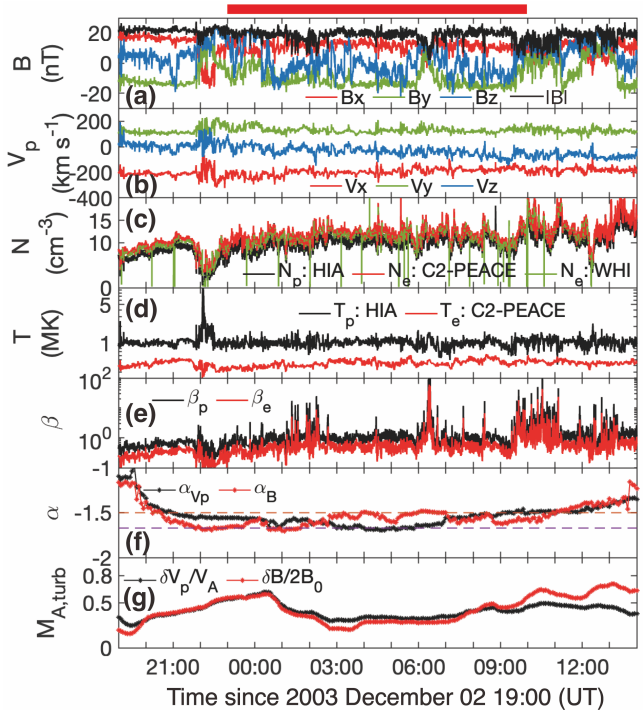


FIG. 1. An overview of fluctuations measured by *Cluster*-1. The red bar on the top marks the interval during 23:00-10:00 UT on 2-3 December 2003. (a) Magnetic field. (b) Proton bulk velocity. (c) Cross-check of proton density from CIS-HIA (black), and electron density from Plasma Electron And Current Experiment (PEACE) [36] onboard *Cluster*-2 (red) and from Waves of High frequency and Sounder for Probing of Electron density by Relaxation (WHISPER) [37] (green). (d,e) Temperature and plasma $\beta$ (the ratio between thermal and magnetic pressures). (f) Moving-window intermediate time series of spectral slopes ($\alpha$) of trace proton velocity and magnetic power. The horizontal dashed lines represent $\alpha = -5/3$ and $-3/2$. (g) $\delta V_p/V_A$ (black) and $\delta B/(2B_0)$ (red), where $\delta V_p$ and $\delta B$ are rms proton velocity and magnetic field fluctuations, respectively.

(GSE) coordinates. During this time interval, the *Cluster* mission is in a tetrahedral-like configuration, with the relative separation $d_{sc} \sim$ 200km (around 3 proton inertial length $d_i \sim$ 74km), enabling us to perform a multi-point analysis on MHD turbulence. Performing an MHD mode decomposition during 23:00-10:00 UT (the red bar on the top of Fig. 1) is applicable for the following reasons. First of all, the background magnetic field measured by the Fluxgate Magnetometer (FGM) [38] and proton plasma parameters measured by the Cluster Ion Spectrometry's Hot Ion Analyzer (CIS-HIA) [39] are relatively stable, as shown in Figs. 1(a-d). Fluctuations are approximately stationary and homogeneous based on the analysis of correlation functions [40]. Additionally, fluctuations are in a well-developed state, as shown in Fig. 1(f) where the spectral slopes ($\alpha_{V_p}$ and $\alpha_B$) of the trace proton velocity and magnetic power at spacecraft-frequency $f_{sc} \sim [0.001Hz, 0.1f_{ci}]$ range between $-5/3$ and $-3/2$ (the proton gyro-frequency $f_{ci} \sim 0.24Hz$). The trace proton velocity and magnetic power are calculated through the fast Fourier transform (FFT) with five-point smoothing in a moving time window with a five-hour length and five-minute moving step. Furthermore, the turbulent Alfvén Mach number is $M_{A,turb} = \delta V_p/V_A \sim 0.3$ (Fig. 1(g)), satisfying the small-amplitude approximation. Table I provides the background parameters used for further analysis.

*MHD mode decomposition.*— We decompose the three MHD eigenmodes by combining three methods: linear decomposition method [21], singular value decomposition (SVD) method [41], and multi-spacecraft timing analysis [42]. This allows direct retrieval of energy wavenumber distributions independent of any spatiotemporal hypothesis (e.g., Taylor hypothesis [43]). We separate compressible fluctuations into slow and fast modes (Alfvén modes are analyzed in [40]) and establish 3D wavenumber distributions in each moving time window. The window length selection (5 hours) provides low-frequency (large-scale) measurements while ensuring $\mathbf{B}_0$ is approaching the local background magnetic field.

First, we obtain wavelet coefficients of proton velocity, magnetic field, and proton density using Morlet-wavelet transforms [42]. Second, wavevector directions ($\hat{\mathbf{k}}_{SVD}(t, f_{sc})$) are calculated using SVD of magnetic wavelet coefficients based on the linearized Gauss's law for magnetism. Third, the $\hat{k}\hat{b}_0$ coordinates are built by $\hat{\mathbf{k}}_{SVD}$, where axis basis vectors are $\hat{\mathbf{e}}_{\parallel} = \hat{\mathbf{b}}_0 = \mathbf{B}_0/|\mathbf{B}_0|$ , $\hat{\mathbf{e}}_{\perp 1} = \hat{\mathbf{k}}_{SVD} \times \hat{\mathbf{b}}_0/|\hat{\mathbf{k}}_{SVD} \times \hat{\mathbf{b}}_0|$, and $\hat{\mathbf{e}}_{\perp 2} = \hat{\mathbf{b}}_0 \times (\hat{\mathbf{k}}_{SVD} \times \hat{\mathbf{b}}_0)/|\hat{\mathbf{b}}_0 \times (\hat{\mathbf{k}}_{SVD} \times \hat{\mathbf{b}}_0)|$. Fourth, power spectra ($P_{\epsilon_l}(t, f_{sc})$) are estimated as the square of wavelet coefficients in $\hat{k}\hat{b}_0$ coordinates, where $\epsilon = V, B, N$ represents proton velocity ($V$), magnetic field ($B$), and proton density ($N$) fluctuations, and $l$ represents $\hat{\mathbf{e}}_{\parallel}$, $\hat{\mathbf{e}}_{\perp 1}$, and $\hat{\mathbf{e}}_{\perp 2}$. Fifth, wavevectors ($\mathbf{k}(t, f_{sc})$) are calculated using the multispacecraft timing analysis [44]. It is worth noting that $\mathbf{k}$ is not entirely aligned with $\hat{\mathbf{k}}_{SVD}$. We present the results under $\eta < 20°$ in the main text, where $\eta$ is the angle between $\mathbf{k}$ and $\hat{k}\hat{b}_0$ plane.

Sixth, we construct a set of $200 \times 200 \times 200$ bins to obtain 3D wavenumber distributions of energy density ($D_{\epsilon_l}(\mathbf{k})$). In each bin, fluctuations have approximately the same wavenumber. To cover all MHD wavenumbers and ensure measurement reliability, we restrict our analysis to fluctuations with $1/(100d_{sc}) < k < 1.1 \times 0.1/d_i$ and $2/t^* < f_{rest} < f_{ci}$, where the wavenumber is $k = \sqrt{k_{\parallel}^2 + k_{\perp}^2}$, $t^*$ is the time window length, $f_{rest} = f_{sc} - \mathbf{k} \cdot \mathbf{V}/2\pi$ is the frequency in the plasma flow frame, and $\mathbf{V}$ is the proton bulk velocity with the spacecraft velocity being negligible. Fluctuations beyond the wavenumber and frequency ranges are set to zero. $D_{\epsilon_l}(\mathbf{k})$ is calculated by averaging $P_{\epsilon_l}(t, f_{sc})$ over effective time points in all time windows and integrating over $f_{sc}$.

Seventh, fast- and slow-mode velocity fluctuations in

TABLE I. Background parameters after replacing the outliers with the linear interpolation of neighboring, non-outlier values.

| Start time (UT) | End time (UT) | $B_0$ (nT) | $N_p$ $(cm^{-3})$ | $V_A$ $(km/s)$ | $V_S$ $(km/s)$ | $\beta_p$ | $V_{Te}$ | $d_i$ | $f_{ci}$ |
|---|---|---|---|---|---|---|---|---|---|
| 2003-12-02/23:00 | 2003-12-03/10:00 | 19.2 | 10.1 | 133 | 121 | 1.0 | 3700 | 74 | 0.24 |

wavevector space are calculated by

$$\delta V_{k,\pm} = \langle |\delta V_{k,\parallel}\hat{\mathbf{e}}_{\parallel} \cdot \hat{\xi}_{\pm} \pm \delta V_{k,\perp 2}\hat{\mathbf{e}}_{\perp 2} \cdot \hat{\xi}_{\pm}| \rangle, \quad (1)$$

where '+' is for fast modes, '−' is for slow modes, and angular brackets denote the time average. Using the random phase approximation, $\delta V_{k,\pm} \propto |\sqrt{D_{V_\parallel}(\mathbf{k})} cos\zeta_{\hat{e}_\parallel \hat{\xi}_\pm} \pm \sqrt{D_{V_{\perp 2}}(\mathbf{k})} sin\zeta_{\hat{e}_\parallel \hat{\xi}_\pm}|$, where $\zeta_{\hat{e}_\parallel \hat{\xi}_\pm}$ is the angle between $\hat{\mathbf{e}}_\parallel$ and $\hat{\xi}_\pm$. Fast- and slow-mode displacement vectors are given by [21]

$$\xi_\pm \propto (-1+\alpha \pm \sqrt{A}) k_\parallel \hat{\mathbf{e}}_\parallel + (1+\alpha \pm \sqrt{A}) k_\perp \hat{\mathbf{e}}_{\perp 2}. \quad (2)$$

The unit displacement vectors are $\hat{\xi}_\pm = \xi_\pm / |\xi_\pm|$. The parameter $A = (1+\alpha)^2 - 4\alpha cos\theta$, where $\alpha = V_S^2/V_A^2$, $V_A$ is the Alfvén speed, $V_S$ is the sound speed, and $\theta$ is the angle between $\mathbf{k}$ and $\mathbf{B}_0$. Fast- and slow-mode magnetic field and proton density fluctuations are estimated as [21]

$$\delta B_{k,\pm} = B_0 \frac{\delta V_{k,\pm}}{V_{ph,\pm}} |\hat{\mathbf{e}}_\parallel \times \hat{\xi}_\pm|, \quad (3)$$

$$\delta N_{k,\pm} = N_0 \frac{\delta V_{k,\pm}}{V_{ph,\pm}} \hat{\mathbf{k}} \cdot \hat{\xi}_\pm. \quad (4)$$

The unit wavevector is $\hat{\mathbf{k}} = \mathbf{k}/|\mathbf{k}|$, and $N_0$ is the background proton density. Fast- and slow-mode phase speeds are given by [45]

$$V_{ph,\pm}^2 = \frac{1}{2}\{(V_S^2+V_A^2) \pm [(V_S^2+V_A^2)^2 - 4V_S^2V_A^2 cos^2\theta]^{1/2}\} \quad (5)$$

Finally, we calculate the energy density of fast and slow modes $D_{\epsilon,\pm} = \delta\epsilon_{k,\pm}^2$. Appendix A presents more method details. Appendix B shows that the decomposed magnetic field and density fluctuations (inferred from proton velocity fluctuations via Eqs. (3,4) [21]) match those directly measured by FGM and CIS-HIA, indicating the reliability of MHD mode decomposition.

*Slow modes.*— In Fig. 2(a), we observe that the normalized wavenumber distributions of the proton velocity energy of slow modes ($\hat{D}_{V-}$; color contours) are prominently distributed along the $k_\perp$ axis, suggesting a faster cascade in the perpendicular direction. We also observe an increase in the anisotropy of energy distributions with the increasing wavenumbers. These observations suggest that smaller eddies of slow modes are more elongated along $\mathbf{B_0}$, in agreement with theoretical expectations and simulation results [18, 23]. The anisotropic behaviors of slow modes found here are roughly similar to those for Alfvén modes, presumably because slow modes passively

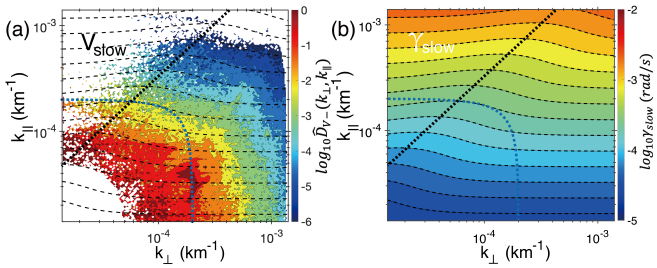


FIG. 2. Slow modes. (a) Wavenumber distributions of $\hat{D}_{V-}$ (color contours) and $\gamma_{slow}$ (black dashed curves). $\hat{D}_{V-} = D_{V-}/D_{V-,max}$ is normalized by the maximum energy density, where $\hat{D}_{V-}$ less than six orders of magnitude or at $k < 5\times10^{-5} km^{-1}$ is set to zero. (b) Slow-mode damping rate ($\gamma_{slow}$). The blue dotted curve in each panel marks an isotropic contour $k = 2\times10^{-4} km^{-1}$. The black dotted line marks the valley line of $\gamma_{slow}$ contours.

mimic Alfvén modes [21, 26]. On top of this anisotropic contour, the $\hat{D}_{V-}$ spectrum exhibits a valley contour along the black dotted line, a notable difference from the Alfvén-mode spectrum that steadily decreases with $k_\perp$ at each $k_\parallel$ [40]. The anisotropy difference between slow and Alfvén modes can be explained by the fact that collisionless damping (CD) can affect slow modes but has little influence on Alfvén modes [3]. To examine this explanation, we estimate slow-mode theoretical damping rate ($\gamma_{slow}$) as a function of $\mathbf{k}$,

$$\gamma_{slow} = \frac{|k|V_S}{2|\cos\theta|}\left(\frac{1}{8}\pi\frac{m_e}{m_p}\right)^{1/2} \left(1 - \frac{\cos 2\theta[(V_S^2/V_A^2)\cos 2\theta - 1]}{[1+V_S^4/V_A^4 - 2(V_S^2/V_A^2)\cos 2\theta]^{1/2}}\right) \quad (6)$$

using the parameters in Table I, where $m_e$ and $m_p$ are the electron and proton mass, respectively [46]. Overall, $\gamma_{slow}$ significantly increases with $k_\parallel$ and has a little change with $k_\perp$ in Fig. 2(b). The contours of $\gamma_{slow}$ (black dashed curves), which is also superposed in Fig. 2(a), perfectly align with the color contours of the $\hat{D}_{V-}$ spectrum along the black dotted line. It suggests that CD can modulate energy distributions of slow modes, and the CD modulation is expected to be more prominent at larger $k_\parallel$ due to the increase of $\gamma_{slow}$. Therefore, wavenumber distributions of slow modes are more stretched perpendicular to $\mathbf{B_0}$ under CD modulation compared to Alfvén modes.

To further estimate the anisotropy of fast (+) and slow

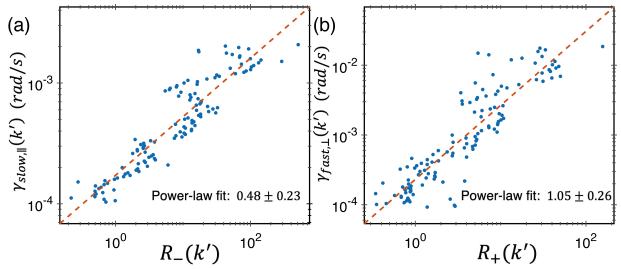


FIG. 3. The relation between the anisotropy of energy distributions ($R_\pm$ estimated by Eq. (7)) and collisionless damping rates. (a) $R_-$ versus $\gamma_{slow,\parallel}$. (b) $R_+$ versus $\gamma_{fast,\perp}$. The red dashed lines represent the power-law fits.

$(-)$ modes, we define a parameter

$$R_\pm(k^{'}) = \frac{D_{V\pm}(k_\perp = k^{'})}{D_{V\pm}(k_\parallel = k^{'})} \tag{7}$$

for a given wavenumber $k^{'}$, where the reduced perpendicular and parallel wavenumber distributions of the energy density are calculated by

$$D_{\epsilon\pm}(k_\perp) \sim \sum_{k_\parallel=k_{low}}^{k_\parallel=k_{upp}} D_{\epsilon\pm}(k_\perp, k_\parallel), \tag{8}$$

$$D_{\epsilon\pm}(k_\parallel) \sim \sum_{k_\perp=k_{low}}^{k_\perp=k_{upp}} D_{\epsilon\pm}(k_\perp, k_\parallel). \tag{9}$$

The integral upper and lower limits are $k_{upp} = 0.1/d_i \sim 1.4\times10^{-3}km^{-1}$ and $k_{low} = 1/(100d_{sc}) \sim 5\times10^{-5}km^{-1}$.

Fig. 3(a) shows a strong correlation between $log_{10}R_-(k^{'})$ and $log_{10}\gamma_{slow,\parallel}(k^{'})$ with the correlation coefficient of 0.92, where the parallel damping rate $\gamma_{slow,\parallel}(k^{'})$ is calculated by averaging $\gamma_{slow}(k_\perp, k_\parallel = k^{'})$ over $k_\perp$ for a given wavenumber $k^{'}$. Moreover, the positive index of power-law fit $(0.48 \pm 0.23)$ indicates that more significant anisotropy of slow modes corresponds to larger values of $\gamma_{slow}$ along $\mathbf{B}_0$.

*Fast modes.*— Different from slow modes, fast modes exhibit CD truncation scales ($kc$) which are obtained by equating the fast-mode cascading rate ($\tau_{fast}^{-1}$) and damping rate ($\gamma_{fast}$), marked by the yellow line in Fig. 4(a). $\tau_{fast}^{-1}$ is defined as $(k/L_0)^{1/2}\delta V_0^2/V_{ph,+}$ [35], where the injection fluctuating velocity $\delta V_0$ is $\sim 40km/s$, the correlation time determined by correlation functions $T_c$ is $\sim 2300s$, and thus the injection scale $L_0$ is $\sim 9.2\times10^4km$. Fig. 4(b) shows that wavenumber distributions of $\tau_{fast}^{-1}$ present an anisotropy independent of scales. When $V_{ph,+}$ $(\sim 100-200km/s)$ is much less than the electron thermal speed $V_{Te}$ $(\sim 3700km/s)$, the fast-mode theoretical damping rate can be estimated as

$$\gamma_{fast} = \frac{|k|V_S}{2|\cos\theta|}\left(\frac{1}{8}\pi\frac{m_e}{m_p}\right)^{1/2} \left(1 + \frac{\cos2\theta[(V_S^2/V_A^2)\cos2\theta - 1]}{[1 + V_S^4/V_A^4 - 2(V_S^2/V_A^2)\cos2\theta]^{1/2}}\right) \tag{10}$$

using the parameters in Table I [46]. Fig. 4(c) shows that $\gamma_{fast}$ sharply enhances with increasing $k_\perp$ and is up to $0.9rad/s$ in the bottom right corner where $\theta$ approaches 90°, indicating that fast modes undergo more severe CD damping and rapid dissipation at larger $k_\perp$ and larger $\theta$.

We superpose the contours of $\tau_{fast}^{-1}$ (black solid curves) and $\gamma_{fast}$ (purple dashed curves) on the normalized wavenumber distributions of the proton velocity energy of fast modes ($\hat{D}_{V+}$; color contours) in Fig. 4(a). The $\hat{D}_{V+}$ spectrum roughly agrees with the contours of $\tau_{fast}^{-1}$ on the left side of the yellow line (above $kc$; $\tau_{fast}^{-1} > \gamma_{fast}$) at $k < 2\times10^{-4}km^{-1}$ (blue dotted curve). The scale-independent, slight anisotropy of the $\hat{D}_{V+}$ spectrum suggests that fast-mode energy distributions do not depend heavily on $\mathbf{B}_0$, consistent with numerical simulations of fast modes [21, 23]. In contrast, at $k > 2\times10^{-4}km^{-1}$, the inverted triangular shape of the $\hat{D}_{V+}$ spectrum (narrowing down at smaller $k_\parallel$) is generally compatible with the triangle contours of $\gamma_{fast}$ on the right side of the yellow line (below $kc$; $\tau_{fast}^{-1} < \gamma_{fast}$), implying the crucial role of $\gamma_{fast}$ in shaping fast-mode energy spectrum. These findings support that energy distributions of plasma turbulence are shaped by the forcing on large scales and damping on small scales.

Fig. 3(b) shows that the correlation coefficient between $log_{10}R_+(k^{'})$ and $log_{10}\gamma_{fast,\perp}(k^{'})$ is 0.90, and their power-law fit is $1.05 \pm 0.26$, where the perpendicular damping rate $\gamma_{fast,\perp}(k^{'})$ is obtained by averaging $\gamma_{fast}(k_\perp = k^{'}, k_\parallel)$ over $k_\parallel$ for a given wavenumber $k'$. This strong correlation between CD and anisotropy of fast modes further indicates that CD plays an increasingly important role in shaping the energy distributions of fast modes as $k_\perp$ increases.

*The relative energy fractions in the total energy of compressible modes.*— Fig. 5 shows the fast-mode energy normalized to the total energy of compressible modes as a function of $k_\perp$ and $\theta$, which is defined as $F_{fast,\epsilon} = \frac{D_{\epsilon+}}{D_{\epsilon+}+D_{\epsilon-}}$. In Fig. 5(a), the fraction of fast-mode energy for the three parameters ($\epsilon = V, B, N$) decreases as $k_\perp$ increases. The similar tendency of the three ratios suggests that CD of compressible modes plays a comparable role at varying $k_\perp$, despite their different energy fractions. Meanwhile, Fig. 5(b) demonstrates that fast modes dominate magnetic field fluctuations, whereas slow modes dominate proton density fluctuations at small $\theta$. As $\theta$ increases, the energy fractions of the three parameters gradually become comparable. Moreover, the linear decrease of $F_{fast,V}$ as $\theta$ increases is consistent with higher $\gamma_{fast}$ at larger $\theta$. The different angle dependencies in $F_{fast,B}$ and $F_{fast,N}$ can be attributed to the angle dependencies in the calculations of their fluctuations from proton velocity fluctuations via Eqs. (3,4).

*Summary.*— This letter presents the first observational proof of substantial CD modulation in the MHD turbulence cascade. Utilizing an improved MHD mode de-

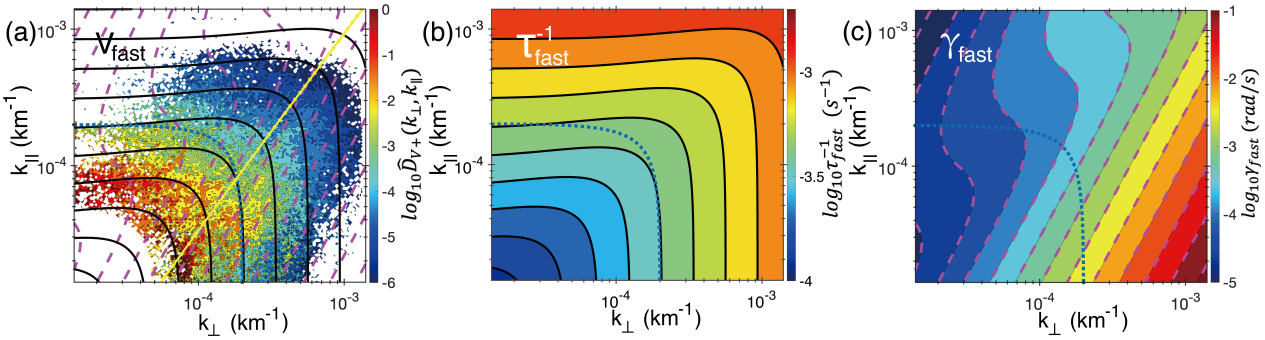


FIG. 4. Fast modes. (a) Wavenumber distributions of $\hat{D}_{V+}$ (color contours), $\tau^{-1}_{fast}$ (black solid curves), and $\gamma_{fast}$ (purple dashed curves). To facilitate the comparison, the velocity energy spectrum is normalized by the same constant as slow modes in Fig. 2(a). $\hat{D}_{V+}$ less than six orders of magnitude or at $k < 5\times10^{-5} km^{-1}$ is set to zero. The yellow line marks the fast-mode CD truncation scales. (b) Fast-mode cascading rate ($\tau^{-1}_{fast}$). (c) Fast-mode damping rate ($\gamma_{fast}$). The blue dotted curve in each panel marks an isotropic contour $k = 2\times10^{-4} km^{-1}$.

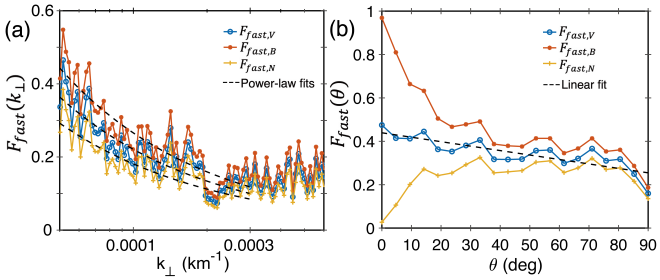


FIG. 5. Fast-mode energy fractions in the total energy of compressible modes. (a) $F_{fast,\epsilon}(k_\perp)$ versus $k_\perp$. (b) $F_{fast,\epsilon}(\theta)$ versus $\theta$. Blue, red, and yellow curves represent energy fractions of proton velocity ($V$), magnetic field ($B$), and proton density ($N$), respectively. The black dashed curves represent the power-law fits of $F_{fast,\epsilon}(k_\perp)$ or linear fit of $F_{fast,V}(\theta)$.

composition technique, we are able to obtain wavenumber distributions of slow and fast modes via four *Cluster* spacecraft measurements in Earth's magnetosheath. Our findings are summarized below:

(1) Wavenumber distributions of slow modes are more stretched perpendicular to $\mathbf{B_0}$ under CD modulation compared to Alfvén modes. In contrast, fast modes are subject to a more significant CD modulation. Fast modes exhibit a scale-independent, slight anisotropy above the CD truncation scales, and their anisotropy increases as the wavenumbers fall below the CD truncation scales, which provides the first observational support for the energy distributions of plasma turbulence shaped by damping on small scales.

(2) Due to the strong pitch angle dependence, CD increases the slow-mode anisotropy along $\mathbf{B}_0$, whereas CD increases the fast-mode anisotropy perpendicular to $\mathbf{B}_0$.

(3) Fast-mode energy fractions in the total energy of compressible modes ($F_{fast,V}$) presents scale- and angle-dependent behaviors, which decrease as $k_\perp$ (or $\theta$) increases.

These observational results are consistent with theoretical expectations [16, 35], which improves understanding of the role of CD in the cascade of compressible turbulence and the corresponding energy transfer, particle transport, and particle energization.

We would like to thank the members of the *Cluster* spacecraft team and NASA's Coordinated Data Analysis Web. The *Cluster* data are available at `https://cdaweb.gsfc.nasa.gov`. Data analysis was performed using the IRFU-MATLAB analysis package available at `https://github.com/irfu/irfu-matlab`. K.H.Y acknowledge the support from the Laboratory Directed Research and Development program of Los Alamos National Laboratory under project number(s) 20220700PRD1.

## Appendix A: Supplementary details of MHD mode decomposition

First, to eliminate the edge effect resulting from finite-length time series, we perform wavelet transforms twice the length of the studied period and cut off the affected periods. Second, the wavevector directions calculated by SVD and background magnetic field are averaged over four *Cluster* spacecraft: $\mathbf{k}_{SVD} = \frac{1}{4}\sum_{i=1,2,3,4}\hat{\mathbf{k}}_{SVD,Ci}$ and $\mathbf{B}_0 = \frac{1}{4}\sum_{i=1,2,3,4}\mathbf{B}_{0,Ci}$. $Ci$ denotes the four *Cluster* spacecraft. Third, $\hat{\mathbf{k}}_{SVD} = \mathbf{k}_{SVD}/|\mathbf{k}_{SVD}|$ and $\hat{\mathbf{b}}_0 = \mathbf{B}_0/|\mathbf{B}_0|$ are used to build $\hat{k}\hat{b}_0$ coordinates, as shown in Fig. 6(a). Fourth, in the analyzed interval, magnetic field data are measured by four *Cluster* spacecraft, whereas proton plasma data are only available on *Cluster*-1. Thus, the magnetic power is calculated by $P_{B_l}(t, f_{sc}) = \frac{1}{4}\sum_{i=1,2,3,4} W_{B_l,Ci}W^*_{B_l,Ci}$. The proton velocity and density power are calculated by $P_{V_l}(t, f_{sc}) = W_{V_l,C1}W^*_{V_l,C1}$ and $P_N(t, f_{sc}) = W_{N,C1}W^*_{N,C1}$. $W_{V_l}$, $W_{B_l}$, and $W_N$ rep-

resent wavelet coefficients of proton velocity, magnetic field, and proton density fluctuations. The subscript $l$ represents $\hat{\mathbf{e}}_{\parallel}$, $\hat{\mathbf{e}}_{\perp 1}$, and $\hat{\mathbf{e}}_{\perp 2}$ directions.

Notice that SVD does not give the magnitude of wavevectors. Therefore, in our fifth step, we utilize the multispacecraft timing analysis based on phase differences between magnetic wavelet coefficients from four spacecraft to determine the wavevectors ($\mathbf{k}_{B_l}(t, f_{sc})$) [44]. We interpolate plasma and magnetic field data to a uniform time resolution of $2^3 samples/s$, to ensure sufficient resolutions for the timing analysis. The phase differences are determined by six cross-correlations for the magnetic field [42], i.e., $W_{B_l}^{12} = \langle W_{B_l,C1} W_{B_l,C2}^* \rangle$, $W_{B_l}^{13} = \langle W_{B_l,C1} W_{B_l,C3}^* \rangle$, $W_{B_l}^{14} = \langle W_{B_l,C1} W_{B_l,C4}^* \rangle$, $W_{B_l}^{23} = \langle W_{B_l,C2} W_{B_l,C3}^* \rangle$, $W_{B_l}^{24} = \langle W_{B_l,C2} W_{B_l,C4}^* \rangle$, and $W_{B_l}^{34} = \langle W_{B_l,C3} W_{B_l,C4}^* \rangle$. The angular brackets denote a time average over $256s$, to obtain reliable phase differences. $\mathbf{k}_{B_l}$ calculated by $l$ ($\hat{\mathbf{e}}_{\parallel}$, $\hat{\mathbf{e}}_{\perp 1}$, and $\hat{\mathbf{e}}_{\perp 2}$) components of the magnetic field is assumed to have no mutual effects at each $t$ and $f_{sc}$. To simplify, we shall write $\mathbf{k}$ as a shorthand notation for $\mathbf{k}_{B_l}$. It is worth noting that $\mathbf{k}$ is not entirely aligned with $\hat{\mathbf{k}}_{SVD}$. Fig. 7 shows wavenumber distributions of proton velocity energy density under $\eta < 10°$, $\eta < 20°$, and $\eta < 30°$, where $\eta$ is the angle between $\mathbf{k}$ and $\hat{k}\hat{b}_0$ plane. We report that the anisotropic signature of fast modes is more prominent when we relax the constraints on $\eta$. It may be because the mode decomposition between slow and fast modes becomes more incomplete when using a more relaxed $\eta$ constraint. Nevertheless, the main properties of energy spectra of slow and fast modes do not significantly change with the increase of $\eta$.

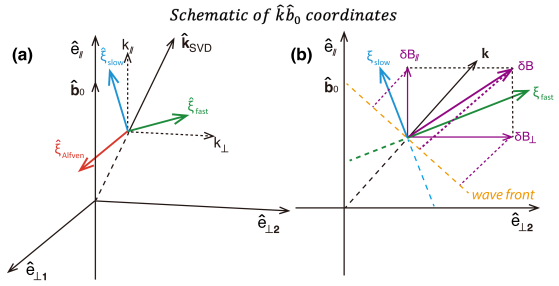


FIG. 6. (a) Schematic of $\hat{k}\hat{b}_0$ coordinates determined by $\hat{\mathbf{k}}_{SVD}$ and $\hat{\mathbf{b}}_0$. The red, blue, and green arrows represent the unit displacement vectors of Alfvén, slow, and fast modes. (b) The composition of magnetic field fluctuations (purple arrow line). The yellow dashed line marks the wave front.

## Appendix B: Examination of MHD mode decomposition

According to the linearized induction equation, the magnetic field within $\hat{k}\hat{b}_0$ plane fluctuates along $\hat{\mathbf{k}} \times (\hat{\mathbf{e}}_{\parallel} \times \hat{\mathbf{k}})$ (along the wave front; yellow dashed line in Fig. 6(b)). The observed magnetic field fluctuations are given by

$$\delta \mathbf{B}_{obs} = \langle |\delta B_{k,\parallel} \hat{\mathbf{e}}_{\parallel} \cdot (\hat{\mathbf{k}} \times (\hat{\mathbf{e}}_{\parallel} \times \hat{\mathbf{k}})) - \delta B_{k,\perp 2} \hat{\mathbf{e}}_{\perp 2} \cdot (\hat{\mathbf{k}} \times (\hat{\mathbf{e}}_{\parallel} \times \hat{\mathbf{k}}))| \rangle. \quad (11)$$

Using the random phase approximation, $\delta \mathbf{B}_{obs} \sim \sqrt{D_{B_{\parallel}}} \hat{\mathbf{e}}_{\parallel} \cdot (\hat{\mathbf{k}} \times (\hat{\mathbf{e}}_{\parallel} \times \hat{\mathbf{k}})) - \sqrt{D_{B_{\perp 2}}} \hat{\mathbf{e}}_{\perp 2} \cdot (\hat{\mathbf{k}} \times (\hat{\mathbf{e}}_{\parallel} \times \hat{\mathbf{k}}))$. The density fluctuations are approximated by $\delta N_{obs} \sim \sqrt{D_N}$. Fig. 8 shows that the decomposed magnetic field and density fluctuations (inferred from proton velocity fluctuations using Eqs. (3,4) [21]) are roughly consistent with those directly measured by FGM and CIS-HIA. Thus, the results of MHD mode decomposition are reliable.

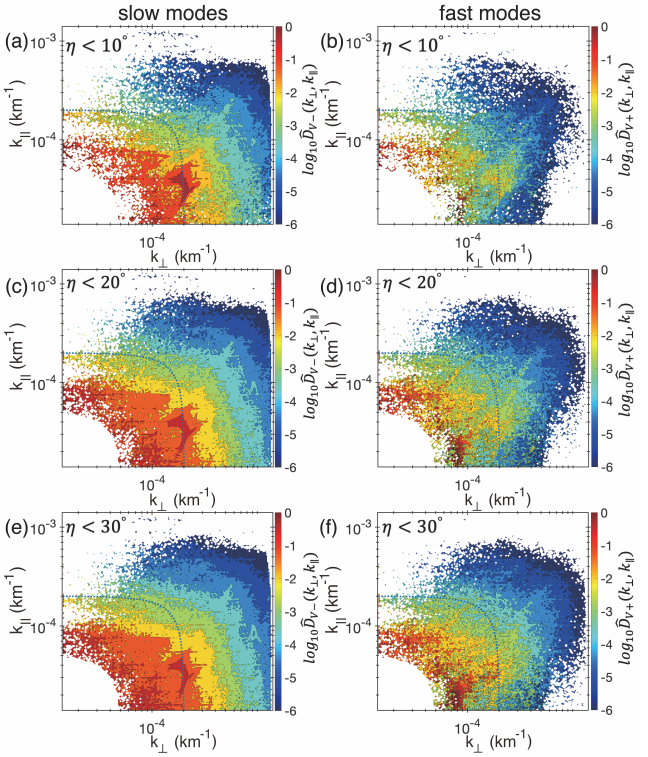


FIG. 7. Wavenumber distributions of proton velocity fluctuations under $\eta < 10°$ (a,b), $\eta < 20°$ (c,d), and $\eta < 30°$ (e,f). (a,c,e) slow-mode spectra. (b,d,f) fast-mode spectra. All spectra are normalized with the maximum energy density to facilitate comparison, where $\hat{D}_{\epsilon\pm}$ less than six orders of magnitude or in the bottom left corner ($k < 5 \times 10^{-5} km^{-1}$) is set to zero. The blue dotted curve in each panel marks an isotropic contour $k = 2 \times 10^{-4} km^{-1}$.

* huirong.yan@desy.de
† terryliuzixu@ucla.edu

[1] R. Bruno and V. Carbone, Living Rev. Sol. Phys. **10**, 2 (2013).
[2] C. Federrath, Phys. Today **71**, 38 (2018).

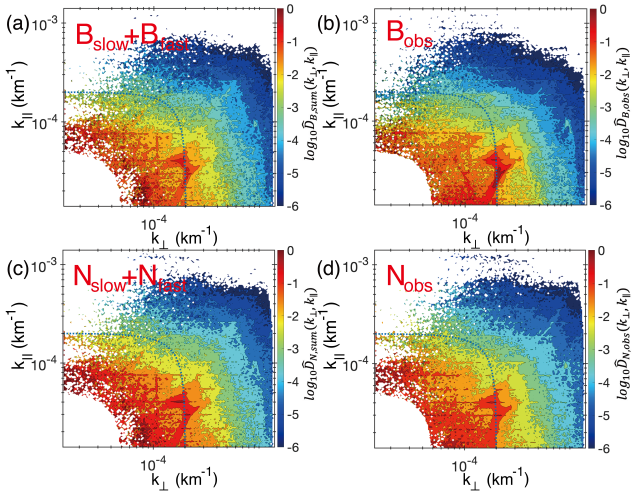


FIG. 8. Wavenumber distributions of decomposed and directly measured results. (a,c) Magnetic field within $\hat{k}\hat{b}_0$ plane and proton density fluctuations from MHD mode decomposition. $D_{B,sum} = D_{B+} + D_{B-}$. $D_{N,sum} = D_{N+} + D_{N-}$. (b,d) Magnetic field within $\hat{k}\hat{b}_0$ plane and proton density fluctuations, measured by FGM and CIS-HIA. Spectrum (b) is normalized four times the constant compared to (a), due to $M_{A,turb} \sim \delta B/2B_0$ (Fig. 1(g)). Spectra (c,d) are normalized with the same constant. All figures use data under $\eta < 20°$.


[3] D. Verscharen, K. G. Klein, and B. A. Maruca, Living Rev. Sol. Phys. **16**, 5 (2019).
[4] H. Yan, in *37th International Cosmic Ray Conference* (2022) p. 38, arXiv:2109.07847 [astro-ph.HE].
[5] W. H. Matthaeus, M. L. Goldstein, and S. R. Lantz, Phys. Fluids **29**, 1504 (1986).
[6] B. D. Chandran, J. Plasma Phys. **84**, 905840106 (2018).
[7] R. Bruno, L. Trenchi, and D. Telloni, Astrophys. J. Lett. **793**, L15 (2014).
[8] K. H. Kiyani, K. T. Osman, and S. C. Chapman, Phil. Trans. R. Soc. A. **373** (2015).
[9] P. Iroshnikov, Astron. Zh. **40**, 742 (1963).
[10] R. H. Kraichnan, Phys. Fluids **8**, 1385 (1965).
[11] P. Goldreich and S. Sridhar, Astrophys. J. **438**, 763 (1995).
[12] G. P. Zank and W. H. Matthaeus, J. Geophys. Res. **97**, 17189 (1992).
[13] G. P. Zank and W. H. Matthaeus, Phys. Fluids **5**, 257 (1993).
[14] A. Barnes, Phys. Fluids **9**, 1483 (1966).
[15] A. Barnes, Phys. Fluids **10(11)**, 2427 (1967).
[16] H. Yan and A. Lazarian, Astrophys. J. **614**, 757 (2004).
[17] T. K. Suzuki, H. Yan, A. Lazarian, and et al., Astrophys. J. **640**, 1005 (2006).
[18] J. Cho and E. T. Vishniac, Astrophys. J. **539**, 273 (2000).
[19] S. Oughton, W. H. Matthaeus, M. Wan, and et al., Phil. Trans. R. Soc. A **373**, 20140152 (2015).
[20] K. Glassmeier, U. Motschmann, and R. Stein, Ann. Geophys. **13**, 76 (1995).
[21] J. Cho and A. Lazarian, MNRAS **345**, 325 (2003).
[22] C. C. Chaston, J. W. Bonnell, S. D. Bale, and et al., Astrophys. J. Suppl. Ser. **246**, 71 (2020).
[23] K. D. Makwana and H. Yan, Phys. Rev. X **10**, 031021 (2020).
[24] X. Zhu, J. He, D. Verscharen, and et al., Astrophys. J. **901**, L3 (2020).
[25] S. Q. Zhao, H. Yan, T. Z. Liu, and et al., Astrophys. J. **923**, 253 (2021).
[26] J. Cho and A. Lazarian, Theor. Comput. Fluid Dyn. **19**, 127 (2005).
[27] S. Q. Zhao, H. Yan, T. Z. Liu, and et al., Astrophys. J. **937**, 102 (2022).
[28] S. Malik, K. H. Yuen, and H. Yan, arxiv.2303.17282 **12**, 1 (2023).
[29] K. H. Yuen, H. Yan, and A. Lazarian, MNRAS **521**, 530 (2023).
[30] Y. Lithwick and P. Goldreich, Astrophys. J. **562**, 279 (2001).
[31] J. Cho and A. Lazarian, Phys. Rev. Lett. **88**, 245001 (2002).
[32] S. Galtier, J. Plasma Phys. **89**, 905890205 (2023).
[33] H. Yan, A. Lazarian, and B. T. Draine, Astrophys. J. **616**, 895 (2004).
[34] V. Petrosian, H. Yan, and A. Lazarian, Astrophys. J. **644**, 603 (2006).
[35] H. Yan and A. Lazarian, Astrophys. J. **673**, 942 (2008).
[36] A. D. Johnstone, C. Alsop, S. Burge, and et al., Space Sci. Rev. **79**, 351 (1997).
[37] P. M. E. Décréau, P. Fergeau, V. Krannosels'kikh, and et al., Space Sci. Rev. **79**, 157 (1997).
[38] A. Balogh, M. W. Dunlop, S. W. H. Cowley, and et al., Space Sci. Rev. **79**, 65 (1997).
[39] H. Rème, C. Aoustin, J. M. Bosqued, and et al., Ann. Geophys. **19**, 1303 (2001).
[40] S. Zhao, H. Yan, T. Z. Liu, and et al., PREPRINT (Version 1) available at Research Square, 10.21203/rs.3.rs-2486073 10.21203/rs.3.rs-2486073 (2023).
[41] O. Santolík, M. Parrot, and F. Lefeuvre, Radio Sci. **38**, 1010 (2003).
[42] A. Grinsted, J. C. Moore, and S. Jevrejeva, Nonlin. Processes Geophys. **11**, 561 (2004).
[43] G. I. Taylor, Proc. R. Soc. Lond. A **164**, 476 (1938).
[44] J.-L. Pincon and K.-H. Glassmeier, ISSI Scientific Report **SR-008**, 91 (1998).
[45] J. V. Hollweg, Rev. Geophys. **13**, 263 (1975).
[46] A. A. Galeev and R. N. Sudan, Plasma Physics, Basic plasma physics **1** (1983).